lubricants

MDPI

Article

Preparation and Tribological Performance of Multi-Layer van der Waals Heterostructure WS_2/h-BN

Yunqi Fang [1], Yang Sun [1,2,*], Fengqin Shang [1], Jing Zhang [1], Jiayu Yao [1], Zihan Yan [1] and Hangyan Shen [1,*]

[1] College of Materials and Chemistry, China Jiliang University, Hangzhou 310018, China
[2] School of Materials Science and Engineering, Tianjin University, Tianjin 300354, China
* Correspondence: yangsun11@cjlu.edu.cn (Y.S.); shenhangyan@cjlu.edu.cn (H.S.)

Abstract: Van der Waals heterostructures with incommensurate contact interfaces show excellent tribological performance, which provides solutions for the development of new solid lubricants. In this paper, a facile electrostatic layer-by-layer self-assembly (LBL) technique was proposed to prepare multi-layer van der Waals heterostructures tungsten disulfide/hexagonal boron nitride (vdWH WS_2/h-BN). The h-BN and WS_2 were modified with poly (diallyldimethylammonium chloride) (PDDA) and sodium dodecyl benzene sulfonate (SDBS) to obtain the positively charged PDDA@h-BN and the negatively charged SDBS@WS_2, respectively. When the mass ratio of PDDA to h-BN and SDBS to WS_2 were both 1:1 and the pH was 3, the zeta potential of PDDA@h-BN and SDBS@WS_2 were 60.0 mV and −50.1 mV, respectively. Under the electrostatic interaction, the PDDA@h-BN and SDBS@WS_2 attracted each other and stacked alternately along the (002) crystal plane forming the multi-layer (four-layer) vdWH WS_2/h-BN. The addition of the multi-layer vdWH WS_2/h-BN (1.0 wt%) to the base oil resulted in a significant reduction of 33.8% in the friction coefficient (0.104) and 16.8% in the wear rate (4.43×10^{-5} $mm^3/(N{\cdot}m)$). The excellent tribological property of the multi-layer vdWH WS_2/h-BN arose from the lattice mismatch (26.0%), a 15-fold higher interlayer slip possibility, and the formation of transfer film at the contact interface. This study provided an easily accessible method for the multi-layer vdWH with excellent tribological properties.

Keywords: van der Waals heterostructure; WS_2/h-BN; electrostatic interaction; layer-by-layer self-assembly; tribological property

check for updates

Citation: Fang, Y.; Sun, Y.; Shang, F.; Zhang, J.; Yao, J.; Yan, Z.; Shen, H. Preparation and Tribological Performance of Multi-Layer van der Waals Heterostructure WS_2/h-BN. *Lubricants* **2024**, *12*, 163. https://doi.org/10.3390/lubricants12050163

Received: 3 March 2024
Revised: 29 April 2024
Accepted: 2 May 2024
Published: 7 May 2024

1. Introduction

Two-dimensional layered materials (2DLMs), such as tungsten disulfide (WS_2) and hexagonal boron nitride (h-BN), are connected via weak van der Waals forces between adjacent layers, making them prone to interlayer slip [1,2]. Based on this property, WS_2 and h-BN are widely used as lubricant additives in fields such as aerospace appliances [1], automobiles [3], and mechanical equipment [4]. By stacking different 2DLMs along the (002) crystal plane, a van der Waals heterostructure (vdWH) can be constructed [5,6]. When sliding along the heterogeneous interface, the vdWH exhibits excellent tribological properties, with a friction coefficient of as low as 0.001 and near-zero wear [7–10]. Given the ultra-low friction coefficient and high wear resistance, the vdWH is expected to become a new lubricant additive.

Presently, the dry transfer method [11], wet transfer method [12], physical vapor deposition (PVD) [13], chemical vapor deposition (CVD) [14], spray-coating process [15], and hydrothermal method [16] are usually used to construct vdWHs. The dry transfer and wet transfer methods were employed for the layer-by-layer transfer of 2DLMs in air and liquid to achieve vdWH stacking. Castellanos et al. [11] proposed a fully dry transfer method that utilizes a viscoelastic stamp to transfer and adhere a single layer of MoS_2 to h-BN, constructing the vdWH MoS_2/h-BN with a thickness 1.5 nm. Dean et al. [12] used poly (methyl methacrylate) as the support layer to transfer graphene to the h-BN

sheet in aqueous solution to form a single-layer vdWH graphene/h-BN. Both the dry transfer and wet transfer methods require the 2DLMs to be transferred and stacked layer by layer, resulting in extremely low preparation efficiency [17]. Dai et al. [13] successfully constructed single-layer vdWH $MoSe_2$/graphene using PVD to deposit $MoSe_2$ directly evaporated on the graphene surface at 650 °C. For the PVD method, $MoSe_2$ layers tend to raise the wrinkles and cracks at high temperatures. Han et al. [18] used CVD to deposit MoS_2 on an h-BN substrate at 1050 °C to construct a single-layer vdWH MoS_2/h-BN. The PVD and CVD methods are primarily suitable for constructing single-layer vdWHs [19], whereas the preparation of multi-layer vdWHs typically necessitates multiple adjustments in reaction sources and pressure. Macknojia et al. [15] sprayed Ti_3C_2TX-MoS_2 onto a steel surface to form a 3.1 μm thick vdWH $Ti_3C_2T_X$-MoS_2 coating. A friction coefficient of 0.003 was demonstrated under test conditions of 20 N and 0.2 m/s. However, the spray method was used to prepare coatings, limiting vdWH to a wide range of applications. Zhao et al. [20] prepared an irregular flower-shaped vdWH WS_2/MoS_2 in a high-pressure reactor at 200 °C using the hydrothermal synthesis method. The hydrothermal synthesis method is challenging in achieving the precise stacking of layered 2DLMs along the direction of the (002) crystal plane due to the difficulty in controlling the growth direction. Furthermore, these methods face challenges in efficiently producing large quantities of multi-layer vdWHs, limiting their applicability in the field of tribology. Therefore, it is necessary to develop simpler and more efficient methods to construct a multi-layer vdWH with multiple heterostructure interfaces.

In this study, electrostatic LBL self-assembly technology was proposed to simply and efficiently prepare a multi-layer vdWH WS_2/h-BN with excellent lubrication properties. PDDA and SDBS as modifiers were used to modify h-BN and WS_2 particles to obtain positively charged PDDA@h-BN and negatively charged SDBS@WS_2, respectively. To enhance the electrostatic interaction between PDDA@h-BN and SDBS@WS_2, the effects of modifier dosage and pH on zeta potential were systematically investigated. Then, the PDDA@h-BN dispersion was mixed with the SDBS@WS_2 dispersion and formed the multi-layer vdWH WS_2/h-BN in a short time. Finally, the tribological behavior of the multi-layer vdWH WS_2/h-BN was investigated, and the lubrication mechanism was revealed.

2. Materials and Methods

2.1. Materials

Hexagonal boron nitride (h-BN, 99.9% pure, 3–5 μm) and tungsten disulfide (WS_2, 99.9% pure, 3–4 μm), provided by Aladdin Reagent Co., Ltd. (Shanghai, China), were used as raw materials for the preparation of a multi-layer vdWH WS_2/h-BN. Figure 1 shows the microstructure and elemental composition of h-BN and WS_2 powders. It can be seen from Figure 1a,b, that the h-BN and WS_2 both had smooth surfaces. In addition, both h-BN and WS_2 had typical layered structures (as indicated with the white arrow) with a thickness of about 0.1–0.2 μm as shown in the inset of Figure 1a,b. Figure 1c,d show the EDS results of the A and B regions, respectively. The h-BN particles were mainly composed of the elements B and N, while the primary elements of WS_2 were W and S. In addition, a certain amount of C was detected on the surfaces of h-BN (10.75 wt%) and WS_2 (12.81 wt%). In addition, poly (diallyldimethylammonium chloride) (PDDA, Ron reagent) and sodium dodecyl benzene sulfonate (SDBS, Aladdin reagent) were used as modifiers to adjust the surface charge of h-BN and WS_2 for a suitable zeta potential.

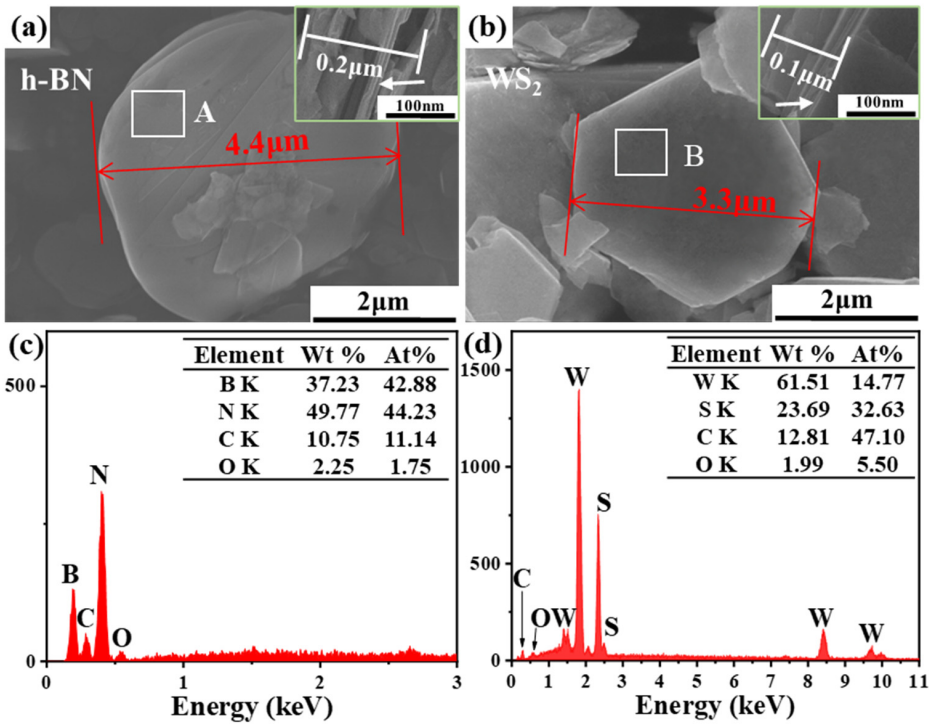

Figure 1. SEM images of (**a**) h-BN and (**b**) WS_2, and EDS results of (**c**) h-BN and (**d**) WS_2. Insets in (**a**,**b**) are the typical layered structure.

2.2. Preparation of Multi-Layer vdWH WS_2/h-BN

The preparation process of a multi-layer vdWH WS_2/h-BN is shown in Figure 2. The preparation included the following two parts:

(1) Synthesis of PDDA@h-BN and SDBS@WS.

The h-BN powder was dispersed in deionized water and a uniform dispersion of 0.2 g/L was formed via sonication for 30 min. Then, PDDA was slowly added to the h-BN dispersion, and the mass ratio of h-BN to PDDA was 1:1, 1:5, 1:10, and 1:15. At the same time, the pH value of the h-BN dispersion was accurately adjusted from 3 to 11 with HCl or NaOH solution, and the reaction system was stirred at 25 °C for 2 h. The obtained product was collected, and the h-BN modified via PDDA was named PDDA@h-BN. WS_2 was modified using SDBS with the same method, and the product was SDBS@WS_2.

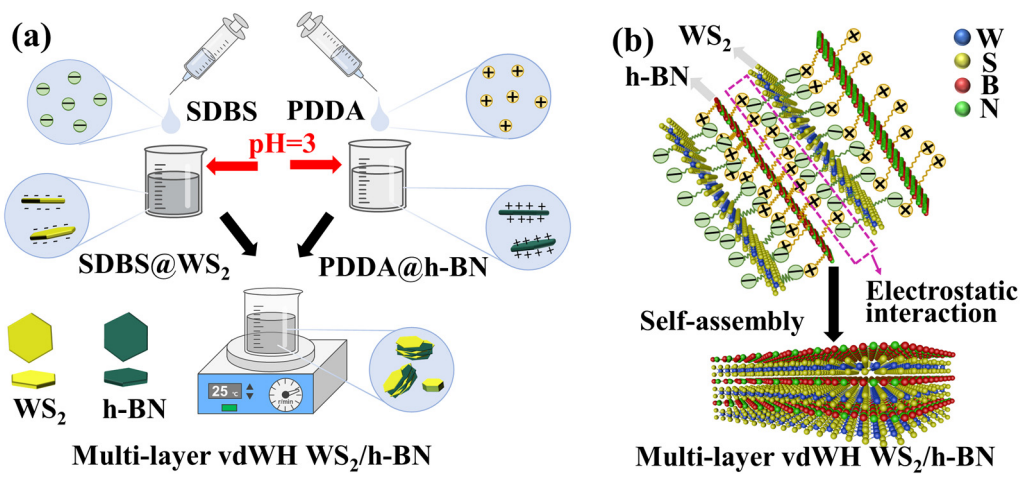

Figure 2. (**a**) The preparation process of a multi-layer vdWH WS_2/h-BN; (**b**) schematic diagram of the process of electrostatic LBL self-assembly of WS_2 and h-BN under electrostatic interaction.

(2) Synthesis of multi-layer vdWH WS_2/h-BN.

As shown in Figure 2b, the positively charged PDDA@h-BN and the negatively charged SDBS@WS_2 realized electrostatic LBL self-assembly through electrostatic interaction. First, PDDA@h-BN and SDBS@WS_2 were dispersed into deionized water to achieve a homogeneous dispersion (0.2 g/L) under sonication. Then, the PDDA@h-BN dispersion was slowly added dropwise to the SDBS@WS_2 dispersion and continuously stirred at 300 rpm for 15 min. Subsequently, it was observed that the negatively charged SDBS@WS_2 and the positively charged PDDA@h-BN flocculated under electrostatic interaction, and quickly settled to the bottom after the stirring was stopped. The precipitate was collected and dried at 60 °C for 6 h to obtain a multi-layer vdWH WS_2/h-BN.

2.3. Characterization

Fourier-transform infrared spectroscopy (FTIR, TENSOR27, Bruker Corporation, Ettlingen, Germany) was used to characterize the surface functional groups before and after the modification of WS_2 and h-BN in the wavenumber range of 4000 to 500 cm^{-1}. The zeta potential of PDDA@h-BN, SDBS@WS_2, and a multi-layer vdWH WS_2/h-BN were measured using the nanoparticle size and a zeta potential analyzer (DLS, Zetasizer Nano ZS90, Malvern Instruments Ltd., Malvern, UK). Before this measurement, the samples were uniformly dispersed in water. The crystal structure of PDDA@h-BN, SDBS@WS_2, and a multi-layer vdWH WS_2/h-BN was examined on an X-ray diffractometer (XRD, X'Pert Pro, PANalytical, Almelo, The Netherlands) with Cu Kα radiation (λ = 0.154 nm) at a step size of 0.06°in the 2θ range of 10–80°. A scanning electron microscope (SEM, SU8010, Hitachi, Ltd., Tokyo, Japan) and an energy-dispersive X-ray spectrometer (EDS, Oxford Instruments, Abingdon, UK) were used to study the microstructure and elemental distribution of a multi-layer vdWH WS_2/h-BN.

2.4. Tribological Tests

In the friction test, commercial 5W40 engine oil (Tianjin Nisseki Lubricating Grease Co., Tianjin, China) was used as the base oil. The multi-layer vdWH WS_2/h-BN (1 wt%) was added to the base oil as an additive, and a uniform dispersion system was obtained via ultrasonication for 10 min and stirring for 30 min. The tribological behavior was examined using a high-speed reciprocating friction and wear tester (HSR-2M, Lanzhou Zhongke Kaihua Technology Development Co., Lanzhou, China) with an applied load of 20 N and a rotating speed of 500 rpm (the corresponding frequency was 8.3 Hz), corresponding with a 2000 m sliding distance. Throughout the test, the upper silicon nitride (Si_3N_4) ball with a diameter of 6 mm slid against the lower fixed 304 stainless steels, and the length of the wear track was kept at 5 mm (l). Then, a probe-type surface profiler (P-6, KLA-Tencor) was utilized to acquire a cross-sectional profile (s) of the wear track. The value of the wear volume (V) was obtained with $V = s \times l$. The wear rate was given via $W = V/(F \times L)$, where W was the wear rate, V was the value of the wear volume, F was the normal load (20 N), and L was the sliding distance [21]. The microstructure and elemental distribution of the wear track were characterized using SEM and EDS to analyze the lubrication mechanism.

3. Results and Discussion

3.1. Subsection Characterization of PDDA@h-BN and SDBS@WS_2

Figure 3 illustrates the impact of modifier dosage and pH on the zeta potential of PDDA@h-BN and SDBS@WS_2, respectively. The relationship between the zeta potential curve and the modifier dosage is shown in Figure 3a. The original zeta potential of h-BN was −26.9 mV. When the mass ratio of h-BN to PDDA was 1:1, h-BN was modified with PDDA to form PDDA@h-BN particles and the surface changed from negatively charged to positively charged with a zeta potential of 53.6 mV. The transformation from a negatively charged surface to a positively charged surface indicated that PDDA had been successfully adsorbed to the h-BN surface. When the mass ratio increased from 1:1 to 1:15, the zeta potential rose from 53.6 mV to 57.3 mV. The original zeta potential of WS_2 was −18.6 mV

and dropped after modification with SDBS. The zeta potential of SDBS@WS_2 was −31.6mV when the mass ratio reached 1:1. Then, the zeta potential stabilized at about −36.6 mV as the amount of SDBS increased (the mass ratio of WS_2 to SDBS was 1:10 and 1:15). The stable zeta potential of SDBS@WS_2 could be attributed to the saturation of SDBS adsorption on the surface of WS_2 [22].

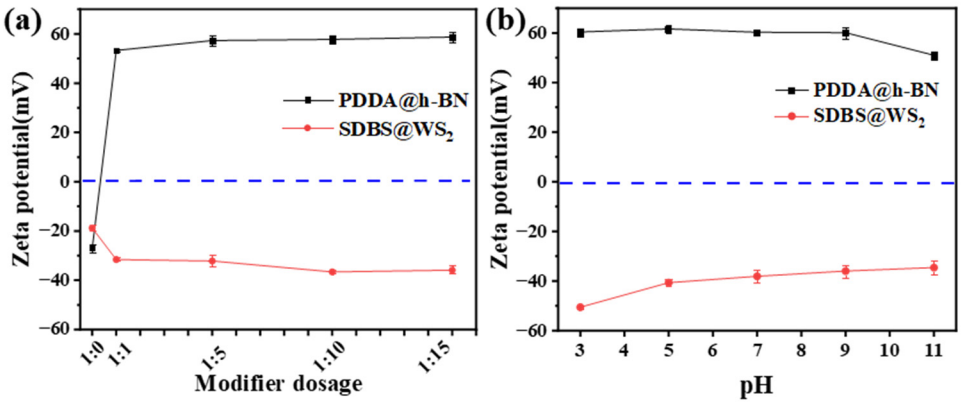

Figure 3. The effect of (**a**) modifier dosage and (**b**) pH on the zeta potential of PDDA@h-BN and SDBS@WS_2.

The above results showed that when the mass ratio reached 1:1, the zeta potential tended to stabilize. Based on this result, the effect of pH on the zeta potential of PDDA@h-BN and SDBS@WS_2, both at a mass ratio of 1:1, is shown in Figure 3b. Interestingly, the zeta potential of PDDA@h-BN and SDBS@WS_2 showed opposite trends with the pH range from 3 to 11. When pH increased from 3 to 9, the zeta potential of PDDA@h-BN remained around 60.0 mV, while the zeta potential rapidly decreased to 51.5 mV at pH = 11. However, the zeta potential of SDBS@WS_2 showed an increasing trend in the pH range from 3 to 11, with the highest electronegativity reaching −50.1 mV at pH = 3. And the zeta potential of SDBS@WS_2 increased to −34.2 mV at pH = 11. Since the pH value of the solution controlled the degree of the protonation of the modifier group, the charge density of PDDA@h-BN and SDBS@WS_2 was greatly increased when pH = 3. In addition, the zeta potential difference between PDDA@h-BN and SDBS@WS_2 reached a maximum value of 110.1 mV at pH = 3, which was beneficial for promoting the attraction and assembly of PDDA@h-BN and SDBS@WS_2 under electrostatic interaction.

The microstructure, EDS, and FTIR spectroscopic results of PDDA@h-BN and SDBS@WS_2 are shown in Figure 4. It can be clearly seen from Figure 4a that a number of irregular particles appeared on the surface of PDDA@h-BN, which was due to the deposition of PDDA on the surface of h-BN (Figure 1a) [23,24]. The EDS results for region A in Figure 4c indicate that PDDA@h-BN was still composed of four elements, B, N, C, and O. Compared with the EDS results of h-BN (Figure 1c), the elemental C content increased significantly from 10.75 wt% (Figure 1c) to 21.66 wt% (Figure 4c), suggesting that PDDA successfully adsorbed on the surface of h-BN. In addition, the elemental C content on the surface of the SDBS@WS_2 increased significantly from 12.81 wt% (Figure 1d) to 21.52 wt% (Figure 4d), which confirmed the adsorption of SDBS particles on the WS_2 surface (Figure 4b).

To confirm that the modifier had been successfully adsorbed on the particle surface, PDDA@h-BN and SDBS@WS_2 were characterized by FTIR. As shown in Figure 4e, h-BN exhibited strong absorption peaks at 1377 cm^{-1} and 817 cm^{-1}, which were attributed to the tensile and bending vibrations of the B-N bond, respectively [25]. PDDA had an unsaturated C=C stretching vibration peak at 1635 cm^{-1}, where the peak at 1473 cm^{-1} belonged to the asymmetric vibration of C-H from N-CH_3, and the absorption peak at 1122 cm^{-1} was caused by C-N bending vibration [26]. The peaks belonging to PDDA appeared at PDDA@h-BN, which indicated that PDDA had been adsorbed onto the surface of h-BN. As shown in Figure 4f, the peak of WS_2 at 1062 cm^{-1} was attributed to the S-S bond

and the peak at 659 cm^{-1} was ascribed to the W-S bond [27]. The peaks at 1010 cm^{-1} and 1190 cm^{-1} corresponded to the S=O and S-O stretching vibrations of SDBS [28]. In addition, the peaks that observed at 1450 cm^{-1} and 835 cm^{-1} were assigned to C=C bonding and C-H out-of-plane bending vibrations in the benzene ring, respectively [28]. Compared to WS_2, peaks belonging to SDBS also appeared in the FTIR spectra of SDBS@WS_2, confirming the adsorption of SDBS on the surface of WS_2. The EDS and FTIR results indicated that PDDA and SDBS had been firmly attached to the surfaces of h-BN and WS_2, making PDDA@h-BN particles positively charged and SDBS@WS_2 particles negatively charged, respectively (Figure 3).

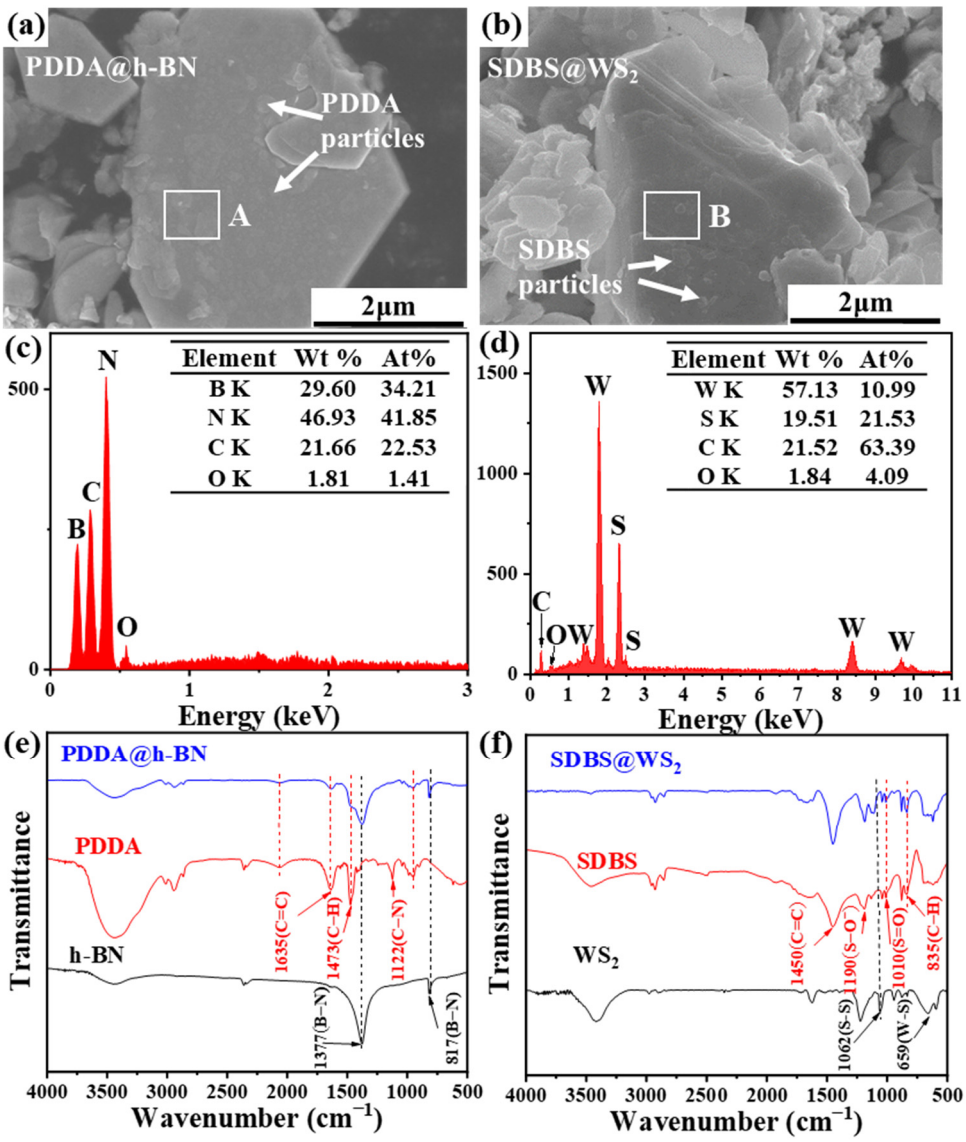

Figure 4. SEM images of (**a**) PDDA@h-BN and (**b**) SDBS@WS_2; EDS results of (**c**) PDDA@h-BN and (**d**) SDBS@WS_2; and FTIR spectra of (**e**) PDDA@h-BN and (**f**) SDBS@WS_2.

3.2. Characterization of Multi-Layer vdWH WS_2/h-BN

Figure 5 presents the dispersion state; zeta potential; and XRD patterns of PDDA@h-BN, SDBS@WS_2, and the multi-layer vdWH WS_2/h-BN. The dispersion states of PDDA@h-BN, SDBS@WS_2, and the multi-layer vdWH WS_2/h-BN in water are shown in Figure 5a. PDDA@h-BN and SDBS@WS_2 were homogeneously dispersed in water for 24 h, showing good dispersion properties. When PDDA@h-BN was added dropwise to SDBS@WS_2, the positively charged PDDA@h-BN and negatively charged SDBS@WS_2 were attracted to each

other through electrostatic interaction, leading to agglomeration. And then, the multi-layer vdWH WS_2/h-BN tended to precipitate to the bottom of the container within 15 min.

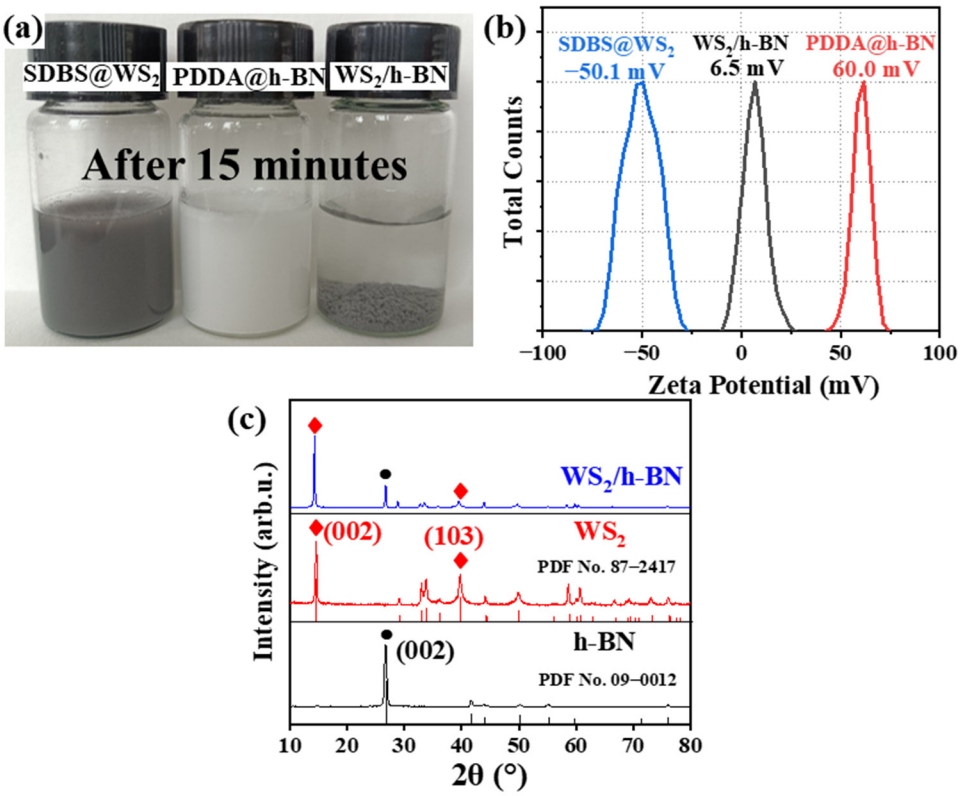

Figure 5. SDBS@WS_2, PDDA@h-BN, and multi-layer vdWH WS_2/h-BN (**a**) dispersion in water, (**b**) zeta potential, and (**c**) XRD pattern.

Zeta potential was an essential parameter for the stability of reactive dispersed systems [29,30]. To identify the reasons for the different dispersion states of PDDA@h-BN, SDBS@WS_2, and the multi-layer vdWH WS_2/h-BN, zeta potential tests were conducted. In Figure 5b, both PDDA@h-BN and SDBS@WS_2 possessed high zeta potential, which were −50.1 mV and 60.0 mV, respectively. Due to the electrostatic repulsion, PDDA@h-BN and SDBS@WS_2 were well dispersed in water to form a stable dispersion. When PDDA@h-BN was mixed with SDBS@WS_2, these two particles self-assembled under the action of electrostatic interaction and formed flocculent precipitates. This phenomenon arose from the electrical neutralization between PDDA@h-BN and SDBS@WS_2, resulting in a decrease in zeta potential to 6.5 mV (Figure 5b). Figure 5c shows the XRD patterns of SDBS@WS_2, PDDA@h-BN, and the multi-layer vdWH WS_2/h-BN. The diffraction peaks at 14.6° and 26.7° corresponded to the (002) crystal plane of WS_2 (PDF No. 87-2417) and the (002) crystal plane of h-BN (PDF No. 09-0012) [20,24], respectively. In addition, all characteristic peaks belonging to WS_2 and h-BN appeared in the multi-layer vdWH WS_2/h-BN.

SEM and EDS were used to investigate the microstructure and elemental composition of the multi-layer vdWH WS_2/h-BN, and the results are shown in Figure 6. It can be seen from Figure 6a that the multi-layer vdWH WS_2/h-BN had a well-stacked layered structure, in which WS_2 was stacked with h-BN along the vertical direction (the (002) crystal plane), forming a sandwich-like structure with four layers of heterogeneous interface. To study the distribution of h-BN and WS_2 in detail, an EDS line scan of the AB line in Figure 6a was performed for the multi-layer vdWH WS_2/h-BN. Figure 6b showed that the distribution of WS_2 and h-BN in the multi-layer vdWH WS_2/h-BN was derived from the variation of the S-element curve and the N-element curve. The line scan result showed that in the structure of the multi-layer vdWH WS_2/h-BN, WS_2 and h-BN were stacked alternately along the

(002) crystal plane with a thickness of 2 μm. According to the above analysis results, the multi-layer vdWHs WS_2/h-BN stacked alternately with WS_2 and h-BN were successfully synthesized under electrostatic interaction between SDBS@WS_2 and PDDA@h-BN.

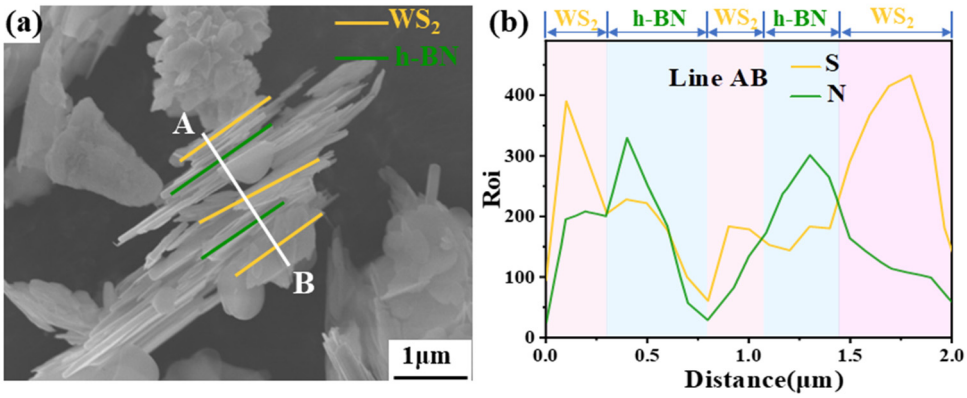

Figure 6. (**a**) SEM image and (**b**) line scan analysis of multi-layer vdWH WS_2/h-BN.

3.3. Tribological Property

The dispersion of the additive in the base oil was essential to ensure its uninterrupted supply to the contact interface. Figure 7 shows the dispersion state of the h-BN, WS_2, the WS_2+h-BN mixture, and the multi-layer vdWH WS_2/h-BN in the base oil after sonication for 10 min and stirring for 30 min. All the additives were evenly dispersed in the base oil for 24 h without precipitation or stratification, indicating the excellent dispersibility of the additives in the base oil. The excellent dispersion stability of the multi-layer vdWH WS_2/h-BN in the base oil ensured its continuous access to the contact interfaces.

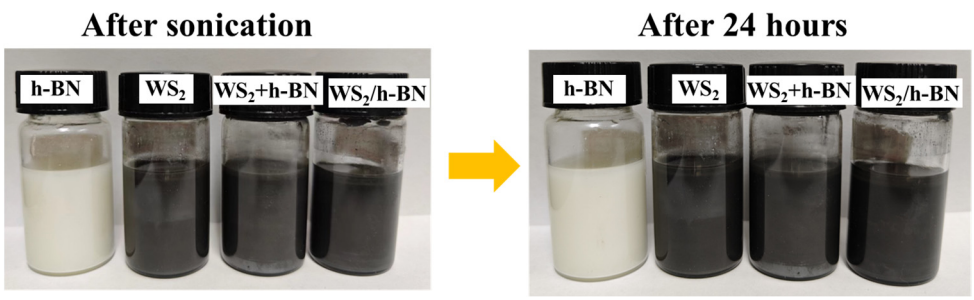

Figure 7. The dispersion states of h-BN, WS_2, WS_2+ h-BN mixture, and vdWH WS_2 h-BN in the base oil for 24 h.

To evaluate the tribological properties of different additives, the multi-layer vdWH WS_2/h-BN, the WS_2, h-BN, and the WS_2+h-BN mixture were added to the base oil, respectively. The tribological property analysis was carried out using a high-speed reciprocating friction and wear tester under a load of 20 N. Figure 8 shows the friction coefficient and wear rate with the additive content of 1.0 wt%, respectively. As shown in Figure 8a, the average friction coefficient of the base oil, WS_2, h-BN, the WS_2+h-BN mixture, and the multi-layer vdWH WS_2/h-BN were 0.157, 0.121, 0.122, 0.147, and 0.104, respectively. After adding WS_2 and h-BN to the base oil, a significant decrease in the friction coefficient was observed. This phenomenon could be attributed to the formation of a continuous transfer film composed of WS_2 and h-BN at the friction interface [31]. What was more important was that the multi-layer vdWH WS_2/h-BN exhibited the lowest friction coefficient, which was reduced by 33% compared to the base oil.

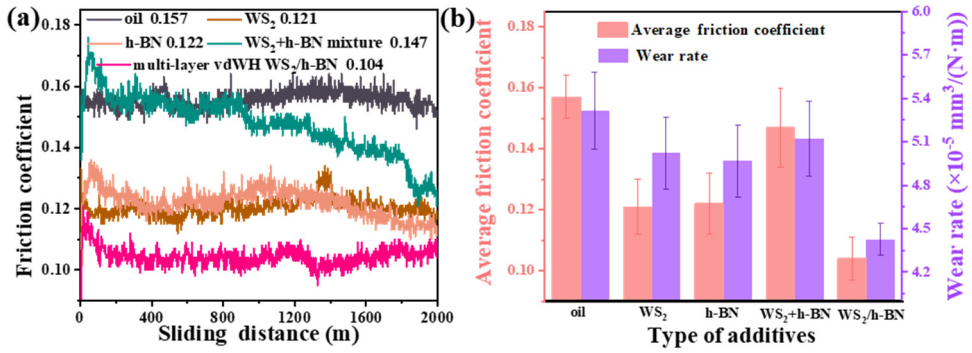

Figure 8. (**a**) The friction coefficient curve and the (**b**) average friction coefficient and wear rate of adding WS_2, h-BN, the WS_2+h-BN mixture, and the multi-layer vdWH WS_2/h-BN to the base oil.

Figure 8b shows the average friction coefficient and wear rate of the base oil and the base oil with four kinds of additives. After adding additives to the base oil, the friction coefficient and wear rate showed a decreasing trend. The wear rates with the additives of WS_2, h-BN, the WS_2+h-BN mixture, and the multi-layer vdWH WS_2/h-BN were 5.02×10^{-5}, 4.97×10^{-5}, 5.12×10^{-5}, and 4.43×10^{-5} $mm^3/(N{\cdot}m)$, respectively. Compared with the base oil, the wear rates were decreased by 5.6%, 6.5%, 3.7%, and 16.8%, respectively. The results suggested that the multi-layer vdWH WS_2/h-BN additive exhibited the lowest friction coefficient and wear rate, significantly improving the tribological properties of the oil lubrication system.

The surface profile and microstructure of the stainless steel (the counter disc), which was lubricated with the base oil, WS_2, h-BN, the WS_2+h-BN mixture, and the multi-layer vdWH WS_2/h-BN, are shown in Figure 9. The wear track lubricated with base oil was the deepest and widest, reaching 28.1 μm and 830.1 μm (Figure 9a_1). There were many grooves and spallings on the wear surface (Figure 9a_3), showing serious abrasive wear. When WS_2, h-BN, and the WS_2+h-BN mixture were added to the base oil, the width of the wear track was reduced to 812.1, 809.8, and 828.7 μm, respectively. At the same time, the depth of the wear track decreased to 27.3, 27.4, and 27.9 μm, respectively. In addition, the deep grooves on the surface of the wear track evolved into shallow grooves, showing slight abrasive wear. Compared with other additives, the wear track of the multi-layer vdWH WS_2/h-BN had the smoothest wear surface. The specific performance was that there were a small number of grooves on the surface of the wear track (Figure 9e_3), and it showed the smallest wear track width (770.9 μm) and wear track depth (25.1 μm), which were 7.1% and 10.7% lower than those of base oil, respectively. The result of the wear track confirmed that multi-layer vdWH WS_2/h-BN had an excellent anti-friction and wear-resistant performance.

In order to understand the evolution of the transfer film, Figure 10 displays the SEM and EDS mappings of the wear track lubricated with the multi-layer vdWH WS_2/h-BN (1.0 wt%) at sliding distances of 200 m and 2000 m. Figure 10a shows a uniform wear track with a smooth surface and the formation of a small amount of transfer film. As the sliding distance increased to 2000 m, the coverage area of the dark area increased significantly and connected together, which indicated the formation of a continuous transfer film, as shown in Figure 10c. The B and N in the transfer film derived from the h-BN in the multi-layer vdWH WS_2/h-BN where the W and S were attributed to WS_2 [32]. As the sliding distance increased from 200 m to 2000 m, the content of WS_2 and h-BN increased from 24.57 wt% to 57.99 wt%, indicating that a continuous transfer film composed of the multi-layer vdWH WS_2/h-BN formed [4,32–34]. During the friction process, the multi-layer vdWH WS_2/h-BN deposits on the surface of the stainless steel and forms a continuous transfer film, thereby reducing friction and the wear of the contact interface [35].

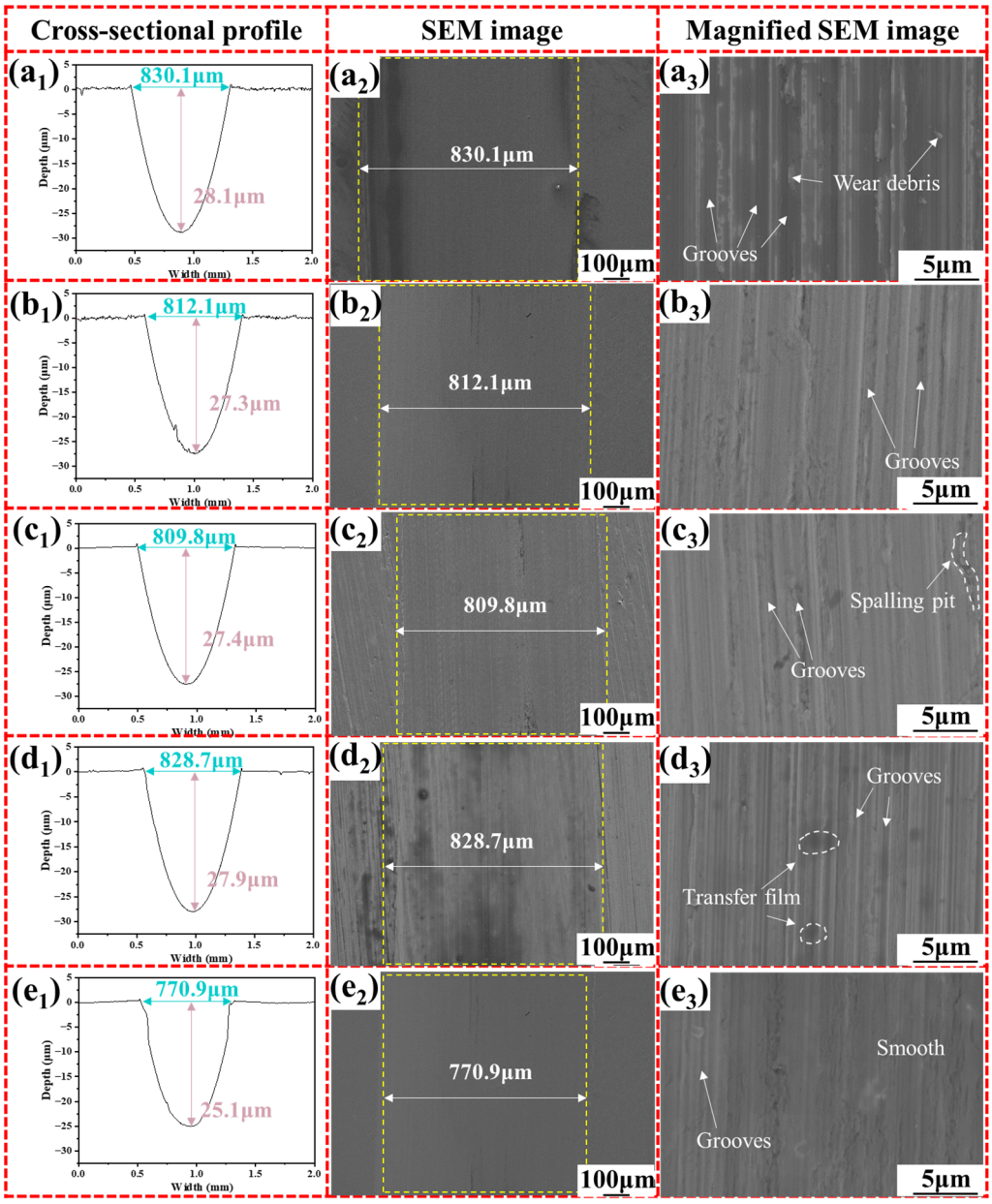

Figure 9. Cross-sectional profile and SEM images of wear tracks of (**a1**–**a3**) oil, (**b1**–**b3**) WS_2, (**c1**–**c3**) h-BN, (**d1**–**d3**) WS_2+h-BN mixture, and (**e1**–**e3**) multi-layer vdWH WS_2/h-BN under a load of 20 N.

3.4. Analysis of Lubrication Mechanism

The lubrication mechanism of the multi-layer vdWH WS_2/h-BN was analyzed as shown in Figure 11a. Firstly, the multi-layer vdWH WS_2/h-BN within the oil is evenly dispersed across the contact area. Under shear forces, these multi-layer vdWHs WS_2/h-BN adhered to the surface of stainless steel and gradually formed a transfer film within the contact area [33]. The EDS analysis of the wear track in Figure 10 confirmed the formation of a transfer film based on the multi-layer vdWH WS_2/h-BN during friction. The transfer film of the multi-layer vdWH WS_2/h-BN with a graphite-like lamellar structure greatly reduced frictional force and improved lubrication performance through interlayer slip [36].

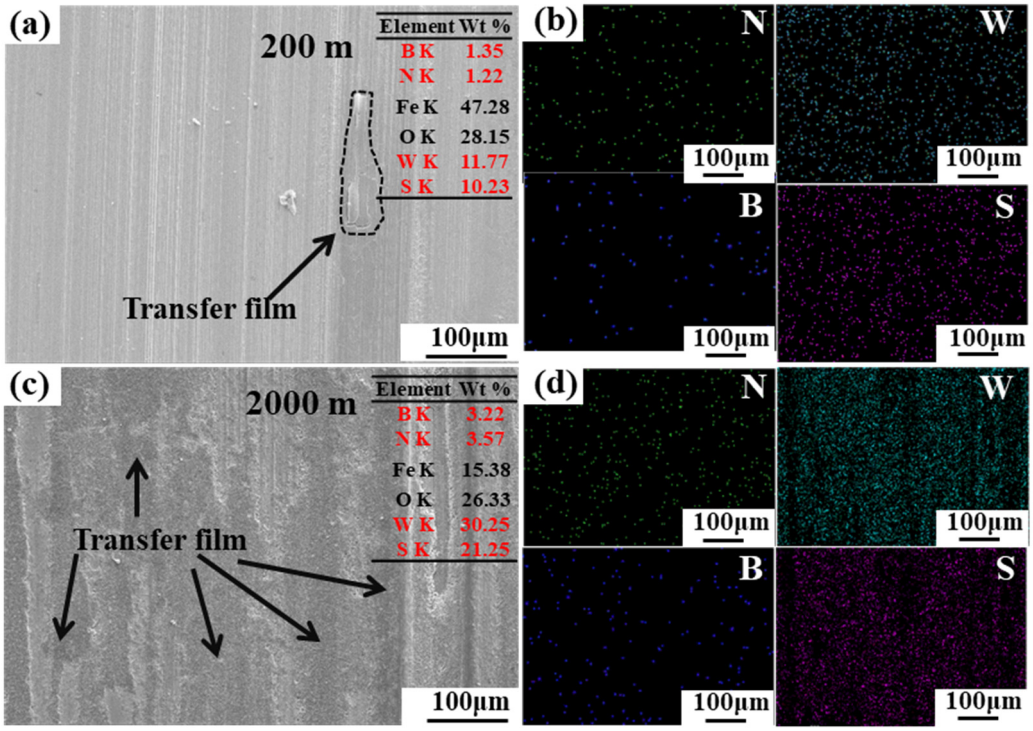

Figure 10. SEM and EDS mappings show the transfer film of multi-layer vdWH WS_2/h-BN after sliding from (**a**,**b**) 200 m to (**c**,**d**) 2000 m.

Furthermore, the lubrication performance of the multi-layer vdWH WS_2/h-BN was much better than that of h-BN, WS_2, and the WS_2+h-BN mixture. It was attributed to the ultra-low interfacial interactions of the multi-layer vdWH WS_2/h-BN. When sliding took place between the layers, WS_2 and h-BN were often firmly locked in a commensurate contact state with strong interfacial interactions due to the no-lattice mismatch characteristics between layers, which results in greater sliding resistance [37,38]. Figure 11b showed that there was a natural lattice mismatch (26.0%) in the multi-layer vdWH WS_2/h-BN due to the different lattice constants between WS_2 (a_1 = 0.315 nm) and h-BN (a_2 = 0.250 nm), which brought the typical incommensurate contact state between layers. This incommensurate contact state induced weak interfacial interactions, making the multi-layer vdWH WS_2/h-BN more prone to interlayer sliding, greatly improving the lubrication performance.

Since interfacial slip was the source of the lubricating properties of layered materials [4,39], the number of slip interfaces would inevitably affect the lubricating properties of layered materials. In order to explore the influence of the number of slip interfaces on the tribological properties of vdWH WS_2/h-BN, the friction and wear properties of single-layer and multi-layer vdWH WS_2/h-BN were shown in Figure 12. Compared with the single-layer vdWH WS_2/h-BN (0.114), the friction coefficient of the multi-layer vdWH WS_2/h-BN (0.104) decreased by 8.7%. Besides, the wear rate of multi-layer vdWH WS_2/h-BN (4.43×10^{-5} $mm^3/(N{\cdot}m)$) was reduced by 8.1% compared to that of single-layer (4.82×10^{-5} $mm^3/(N{\cdot}m)$). The multi-layer vdWH WS_2/h-BN with alternating stacks of WS_2 and h-BN had more heterogeneous interfaces than single-layer vdWH WS_2/h-BN which allowed to undergo multi-slip in the slip process. Figure 13 shows the slip probability of the single-layer and multi-layer vdWH WS_2/h-BN slip system. It could be seen that single-layer vdWH WS_2/h-BN had just one heterogeneous interface, and a single slip could be performed during the slip process. Multi-layer (4 layers) vdWH WS_2/h-BN with 4 heterogeneous interfaces could slide along one or more heterogeneous interfaces at the same time during the slip process, which owned a total of 15 slip states. When interlayer slip occurred, the slip probability of the multi-layer vdWH WS_2/h-BN was 15 times higher than that of the single-layer vdWH WS_2/h-BN. Therefore, the multi-layer vdWH WS_2/h-

BN with multiple heterogeneous interfaces exhibited a greater possibility of interlayer sliding [36,40], and had superior tribological property.

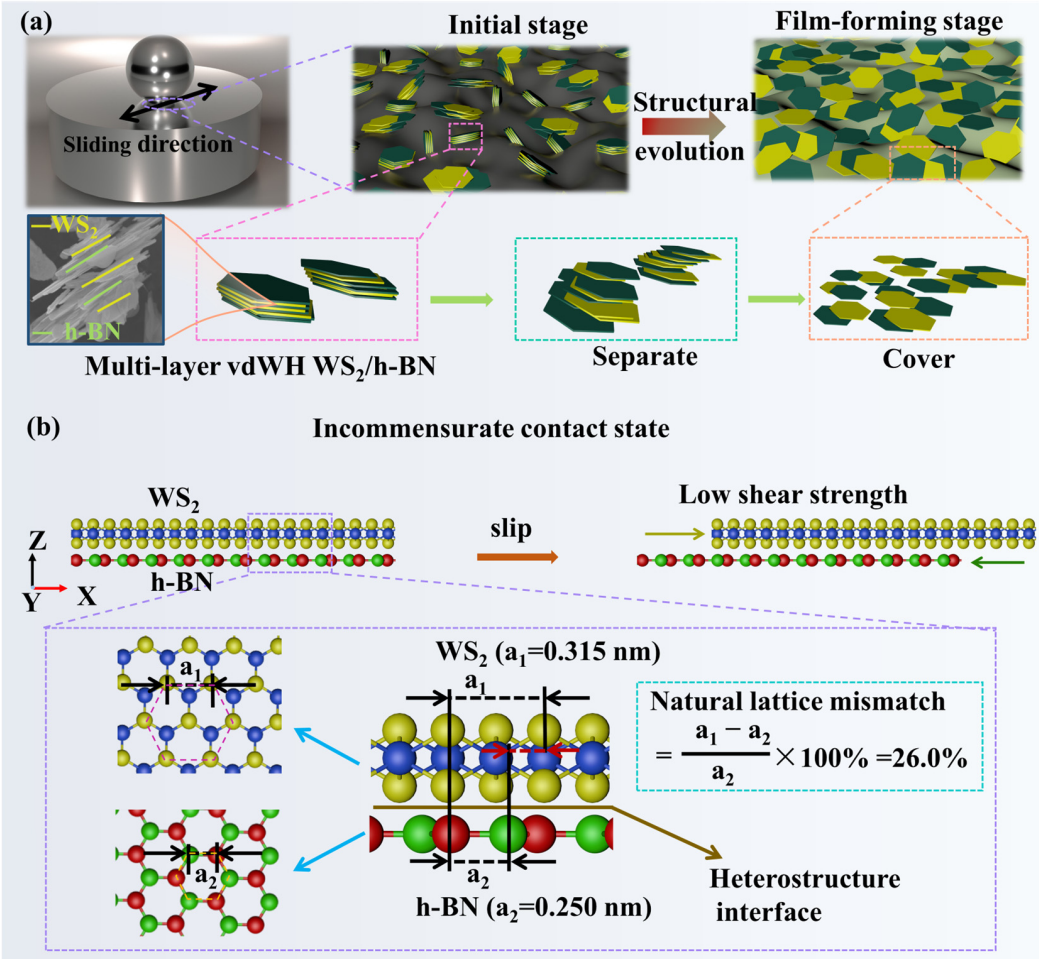

Figure 11. (**a**) Schematic diagram of the lubrication mechanisms of the multi-layer vdWH WS_2/h-BN and (**b**) the state of interlayer slips of the multi-layer vdWH WS_2/h-BN.

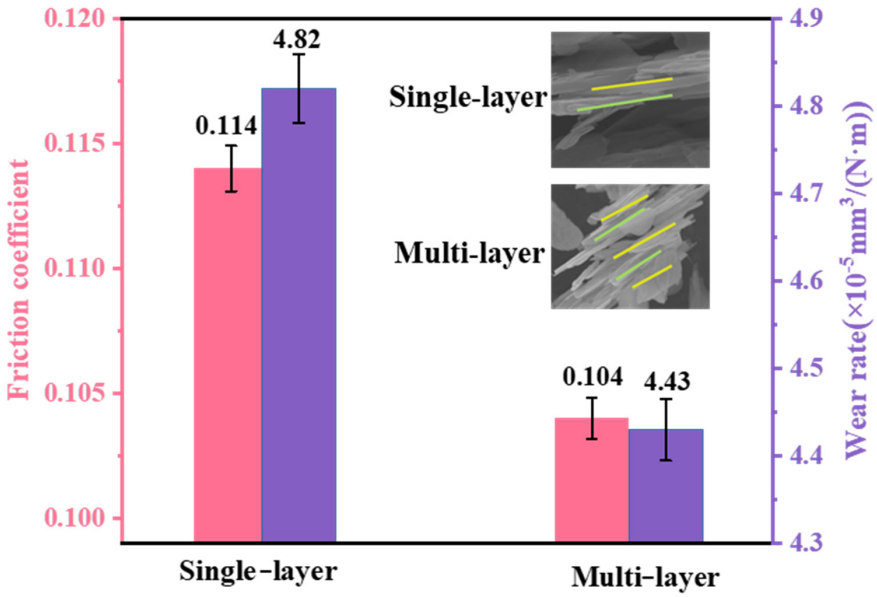

Figure 12. The friction and wear properties of single-layer and multi-layer vdWH WS_2/h-BN.

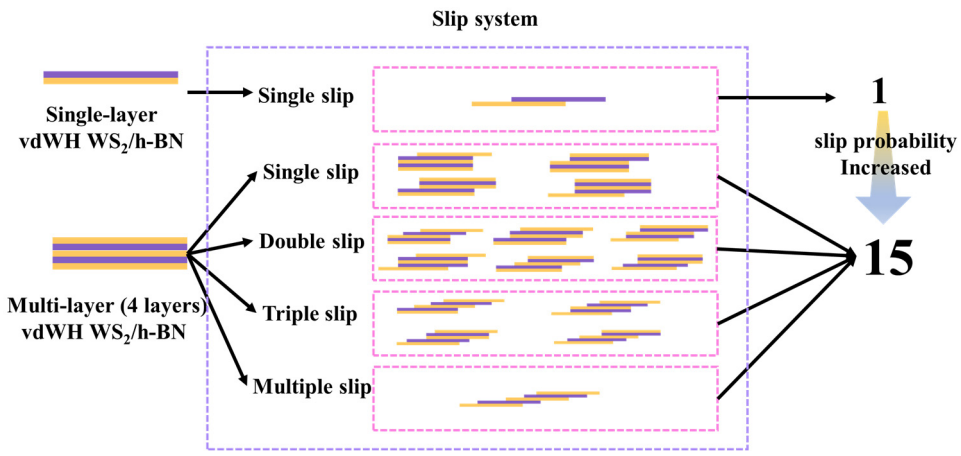

Figure 13. Schematic diagram of single-layer and multi-layer vdWH WS_2/h-BN slip system.

4. Conclusions

The multi-layer vdWH WS_2/h-BN with alternating stacking of WS_2 and h-BN was successfully prepared by electrostatic LBL self-assembly technology. The effects of modifier dosage and pH on the zeta potential of h-BN and WS_2 were systematically investigated. In addition, the tribological behavior and lubricating mechanism of multi-layer vdWH WS_2/h-BN were studied, respectively.

(1) SDBS and PDDA were used to modify WS_2 and h-BN, which the negatively charged SDBS@WS_2 and the positively charged PDDA@h-BN were successfully prepared. When the mass ratio of h-BN to PDDA was 1:1 and pH = 3, the zeta potential of PDDA@h-BN was 60.0 mV. Under the same conditions, the zeta potential of SDBS@WS_2 was −50.1 mV.

(2) The multi-layer (4 layers) vdWH WS_2/h-BN synthesized by electrostatic interaction method had a sandwich-like structure, in which WS_2 and h-BN were stacked alternately along the (002) crystal plane.

(3) Compared with the base oil, the addition of multi-layer vdWH WS_2/h-BN (1.0 wt%) reduced the friction coefficient (0.104) by 33.8% and the wear rate (4.43×10^{-5} $mm^3/(N{\cdot}m)$) by 16.8%. This arose from a natural lattice mismatch of 26.0% between the heterogeneous interfaces in multi-layer vdWH WS_2/h-BN.

(4) The multi-layer (4 layers) vdWH WS_2/h-BN had better tribological property than single-layer vdWH WS_2/h-BN. The friction coefficient (0.104) and wear rate (4.43×10^{-5} $mm^3/(N{\cdot}m)$) were 8.7% and 8.1% lower than those of single-layer vdWH WS_2/h-BN, respectively. This was due to the fact that multi-layer vdWH WS_2/h-BN provided more heterogeneous interfaces, which made its slip probability 15 times higher than that of single-layer vdWH WS_2/h-BN.

Author Contributions: Y.F.: Methodology, Investigation, Data Curation, Writing—Original Draft; Y.S.: Funding Acquisition, and Writing—Review and Editing; F.S.: Methodology and Supervision; J.Z.: Investigation and Methodology; J.Y.: Validation. Z.Y.: Conceptualization; H.S.: Conceptualization, Resources, Supervision, and Writing—Review and Editing. All authors have read and agreed to the published version of the manuscript.

Funding: The research was supported by the National College Students Innovation and Entrepreneurship Training Program (202310356034), the Zhejiang Provincial Natural Science Foundation (LQ24E040001) and Science and Technology Innovation Activity Program for College Students in Zhejiang Province (New Seedling Talent Program) Project (2024R409043).

Data Availability Statement: The data presented in this study are available in the article.

Conflicts of Interest: The authors declare no conflicts of interest.

References

1. Tu, Y.; Zhang, L.; Zhang, X.; Kang, X. Improving the mechanical and tribological behavior of Cu-WS_2 self-lubricating composite with the addition of WS_2 nanosheet. *Wear* **2023**, *530–531*, 205013. [CrossRef]
2. Zhang, D.; Li, Z.; Klausen, L.H.; Li, Q.; Dong, M. Friction behaviors of two-dimensional materials at the nanoscale. *Mater. Today Phys.* **2022**, *27*, 100771. [CrossRef]
3. Aldana, P.U.; Dassenoy, F.; Vacher, B.; Mogne, T.L.; Thiebaut, B.; Bouffet, A. Antispalling Effect of WS_2 Nanoparticles on the Lubrication of Automotive Gearboxes. *Tribol. Trans.* **2016**, *59*, 178–188. [CrossRef]
4. Kumari, S.; Chouhan, A.; Siva Kumar Konathala, L.N.; Sharma, O.P.; Ray, S.S.; Ray, A.; Khatri, O.P. Chemically functionalized 2D/2D hexagonal boron Nitride/Molybdenum disulfide heterostructure for enhancement of lubrication properties. *Appl. Surf. Sci.* **2022**, *579*, 152157–152168. [CrossRef]
5. Novoselov, K.S.; Mishchenko, A.; Carvalho, A.; Neto, A.H.C. 2D materials and van der Waals heterostructures. *Science* **2016**, *353*, 9439. [CrossRef] [PubMed]
6. Geim, A.K.; Grigorieva, I.V. Van der Waals heterostructures. *Nature* **2013**, *499*, 419–425. [CrossRef] [PubMed]
7. Song, Y.; Mandelli, D.; Hod, O.; Urbakh, M.; Ma, M.; Zheng, Q. Robust microscale superlubricity in graphite/hexagonal boron nitride layered heterojunctions. *Nat. Mater.* **2018**, *17*, 894–899. [CrossRef] [PubMed]
8. Mandelli, D.; Leven, I.; Hod, O.; Urbakh, M. Sliding friction of graphene/hexagonal-boron nitride heterojunctions: A route to robust superlubricity. *Sci. Rep.* **2017**, *7*, 10851. [CrossRef] [PubMed]
9. Liao, M.; Nicolini, P.; Du, L.; Yuan, J.; Wang, S.; Yu, H.; Tang, J.; Cheng, P.; Watanabe, K.; Taniguchi, T.; et al. UItra-low friction and edge-pinning effect in large-lattice-mismatch van der Waals heterostructures. *Nat. Mater.* **2022**, *21*, 47–53. [CrossRef]
10. Tian, J.; Yin, X.; Li, J.; Qi, W.; Huang, P.; Chen, X.; Luo, J. Tribo-Induced Interfacial Material Transfer of an Atomic Force Microscopy Probe Assisting Superlubricity in a WS_2/Graphene Heterojunction. *ACS Appl. Mater. Interfaces* **2019**, *12*, 4031–4040. [CrossRef]
11. Wei, Z.; Li, B.; Xia, C.; Cui, Y.; He, J.; Xia, J.-B.; Li, J. Various Structures of 2D Transition-Metal Dichalcogenides and Their Applications. *Small Methods* **2018**, *2*, 1800094. [CrossRef]
12. Dean, C.R.; Young, A.F.; Meric, I.; Lee, C.; Wang, L.; Sorgenfrei, S.; Watanabe, K.; Taniguchi, T.; Kim, P.; Shepard, K.L.; et al. Boron nitride substrates for high-quality graphene electronics. *Nat. Nanotechnol.* **2010**, *5*, 722–726. [CrossRef] [PubMed]
13. Dai, T.-J.; Chen, Y.-Q.; Zhou, Z.-Y.; Sun, J.; Peng, X.-S.; Liu, X.-Z. Two-dimensional $MoSe_2$/graphene heterostructure thin film with wafer-scale continuity via van der Waals epitaxy. *Chem. Phys. Lett.* **2020**, *755*, 137762. [CrossRef]
14. Han, T.; Liu, H.; Wang, S.; Chen, S.; Yang, K. The Large-Scale Preparation and Optical Properties of MoS_2/WS_2 Vertical Hetero-Junction. *Molecules* **2020**, *25*, 1857. [CrossRef] [PubMed]
15. Macknojia, A.; Ayyagari, A.; Zambrano, D.; Rosenkranz, A.; Shevchenko, E.V.; Berman, D. Macroscale Superlubricity Induced by MXene/MoS_2 Nanocomposites on Rough Steel Surfaces under High Contact Stresses. *ACS Nano* **2023**, *17*, 2421–2430. [CrossRef] [PubMed]
16. Man, X.; Liang, P.; Shu, H.; Zhang, L.; Wang, D.; Chao, D.; Liu, Z.; Du, X.; Wan, H.; Wang, H. Interface Synergistic Effect from Layered Metal Sulfides of MoS_2/SnS_2 van der Waals Heterojunction with Enhanced Li-Ion Storage Performance. *J. Phys. Chem. C* **2018**, *122*, 24600–24608. [CrossRef]
17. Yu, X.; Wang, X.; Zhou, F.; Qu, J.; Song, J. 2D van der Waals Heterojunction Nanophotonic Devices: From Fabrication to Performance. *Adv. Funct. Mater.* **2021**, *31*, 2104260. [CrossRef]
18. Han, T.; Liu, H.; Chen, S.; Chen, Y.; Wang, S.; Li, Z. Fabrication and Characterization of MoS_2/h-BN and WS_2/h-BN Heterostructures. *Micromachines* **2020**, *11*, 1114–1130. [CrossRef]
19. Purbayanto, M.A.K.; Chandel, M.; Birowska, M.; Rosenkranz, A.; Jastrzębska, A.M. Optically Active MXenes in Van der Waals Heterostructures. *Adv. Mater.* **2023**, *35*, e2301850. [CrossRef]
20. Zhao, Y.; Liu, J.; Zhang, X.; Wang, C.; Zhao, X.; Li, J.; Jin, H. Convenient Synthesis of WS_2/MoS_2 Heterostructures with Enhanced Photocatalytic Performance. *J. Phys. Chem. C* **2019**, *123*, 27363–27368. [CrossRef]
21. Ren, K.; Yu, G.; Zhang, Z.; Wu, W.; Tian, P.; Chhattal, M.; Gong, Z.; Li, Y.; Zhang, J. Self-organized transfer film-induced ultralow friction of Graphene/$MoWS_4$ heterostructure nanocomposite. *Appl. Surf. Sci.* **2022**, *572*, 151443. [CrossRef]
22. Ni, X.; Li, Z.; Wang, Y. Adsorption Characteristics of Anionic Surfactant Sodium Dodecylbenzene Sulfonate on the Surface of Montmorillonite Minerals. *Front. Chem.* **2018**, *6*, 390–400. [CrossRef]
23. Wang, X.; Wang, X.; Zhao, J.; Song, J.; Su, C.; Wang, Z. Surface modified TiO_2 floating photocatalyst with PDDA for efficient adsorption and photocatalytic inactivation of Microcystis aeruginosa. *Water Res.* **2018**, *131*, 320–333. [CrossRef] [PubMed]
24. Shen, H.; Guo, J.; Wang, H.; Zhao, N.; Xu, J. Bioinspired modification of h-BN for high thermal conductive composite films with aligned structure. *ACS Appl. Mater. Interfaces* **2015**, *7*, 5701–5709. [CrossRef]
25. Sui, Y.; Li, P.; Dai, X.; Zhang, C. Green self-assembly of h-BN@PDA@MoS_2 nanosheets by polydopamine as fire hazard suppression materials. *React. Funct. Polym.* **2021**, *165*, 105965–105977. [CrossRef]
26. Lv, F.; Lu, X.; Song, J.; Zhu, M.; Wang, S.; Xu, Y.; Chang, X. Enhanced Aramid/Al_2O_3 interfacial properties by PDDA modification for the preparation of composite insulating paper. *Res. Chem. Intermed.* **2022**, *48*, 4815–4835. [CrossRef]
27. Vaziri, H.S.; Shokuhfar, A.; Afghahi, S.S.S. Synthesis of WS_2/CNT hybrid nanoparticles for fabrication of hybrid aluminum matrix nanocomposite. *Mater. Res. Express* **2020**, *7*, 025034–025048. [CrossRef]
28. Allahbakhsh, A.; Haghighi, A.H.; Sheydaei, M. Poly(ethylene trisulfide)/graphene oxide nanocomposites. *J. Therm. Anal. Calorim.* **2016**, *128*, 427–442. [CrossRef]

29. Cho, E.-C.; Chang-Jian, C.-W.; Zheng, J.-H.; Huang, J.-H.; Lee, K.-C.; Ho, B.-C.; Hsiao, Y.-S. Microwave-assisted synthesis of TiO_2/WS_2 heterojunctions with enhanced photocatalytic activity. *J. Taiwan Inst. Chem. Eng.* **2018**, *91*, 489–498. [CrossRef]
30. Shu, D.; Li, Y.; Liu, A.; Zhang, H.; Zhou, Y. Facile route to preparation of positively charged GO using poly (diallyldimethylammoniumchloride). *Fuller. Nanotub. Carbon Nanostruct.* **2019**, *28*, 394–401. [CrossRef]
31. Zhang, X.; Xu, H.; Wang, J.; Ye, X.; Lei, W.; Xue, M.; Tang, H.; Li, C. Synthesis of ultrathin WS_2 nanosheets and their tribological properties as lubricant additives. *Nanoscale Res. Lett.* **2016**, *11*, 442–451. [CrossRef] [PubMed]
32. Fan, X.; Li, X.; Zhao, Z.; Yue, Z.; Feng, P.; Ma, X.; Li, H.; Ye, X.; Zhu, M. Heterostructured rGO/MoS_2 nanocomposites toward enhancing lubrication function of industrial gear oils. *Carbon* **2022**, *191*, 84–97. [CrossRef]
33. Feng, P.; Ren, Y.; Li, Y.; He, J.; Zhao, Z.; Ma, X.; Fan, X.; Zhu, M. Synergistic lubrication of few-layer $Ti_3C_2T_x/MoS_2$ heterojunction as a lubricant additive. *Friction* **2022**, *10*, 2018–2032. [CrossRef]
34. Neves, G.O.; Araya, N.; Salvaro, D.B.; Lamim, T.d.S.; Giacomelli, R.O.; Binder, C.; Klein, A.N.; de Mello, J.D.B. Tribologically induced nanostructural evolution of carbon materials: A new perspective. *Friction* **2023**, *12*, 144–163. [CrossRef]
35. Shao, X.; Wang, L.; Yang, Y.; Yang, T.; Deng, G.; He, Y.; Dong, L.; Wang, H.; Yang, J. Influence of preload on the tribological performance of MoS_2/GO composite lubricating coating. *Tribol. Int.* **2023**, *181*, 108306. [CrossRef]
36. Kong, S.; Wang, J.; Hu, W.; Li, J. Effects of Thickness and Particle Size on Tribological Properties of Graphene as Lubricant Additive. *Tribol. Lett.* **2020**, *68*, 112–122. [CrossRef]
37. Hod, O.; Meyer, E.; Zheng, Q.; Urbakh, M. Structural superlubricity and ultralow friction across the length scales. *Nature* **2018**, *563*, 485–492. [CrossRef] [PubMed]
38. Liu, Y.; Grey, F.; Zheng, Q. The high-speed sliding friction of graphene and novel routes to persistent superlubricity. *Sci. Rep.* **2014**, *4*, 4875–4882. [CrossRef]
39. Li, C.; Yu, Y.; Ding, Q.; Yang, L.; Liu, B.; Bai, L. Enhancement on lubrication performances of water lubricants by multilayer graphene. *Tribol. Lett.* **2023**, *72*, 5–25. [CrossRef]
40. Liang, H.; Chen, X.; Bu, Y.; Xu, M.; Zheng, G.; Gao, K.; Hua, X.; Fu, Y.; Zhang, J. Macroscopic superlubricity of potassium hydroxide solution achieved by incorporating in-situ released graphene from friction pairs. *Friction* **2022**, *11*, 567–579. [CrossRef]